Optical analog-signal transmission system in a dynamic and complex scattering environment using binary encoding with a modified differential method

YONGGUI CAO,[1] (iD) YIN XIAO,[1] (iD) AND WEN CHEN[1,2,*] (iD)

[1]*Department of Electronic and Information Engineering, The Hong Kong Polytechnic University, Hong Kong, China*
[2]*Photonics Research Institute, The Hong Kong Polytechnic University, Hong Kong, China*
*owen.chen@polyu.edu.hk

Abstract: High-fidelity optical transmission through dynamic scattering media is challenging, since transmission errors are induced due to dynamic scattering media. In this paper, a new scheme is proposed to realize high-fidelity free-space optical analog-signal transmission in dynamic and complex scattering environments using binary encoding with a modified differential method. Each pixel of an analog signal to be transmitted is first divided into two values, and each of them is encoded into a random matrix. Then, a modified error diffusion algorithm is utilized to transform the random matrix into a 2D binary array. Each pixel of the analog signal to be transmitted is eventually encoded into only two 2D binary arrays, and transmission errors and dynamic scaling factors induced by dynamic and complex scattering media can be temporally corrected. Dynamic smoke and non-line-of-sight (NLOS) are created as a dynamic and complex scattering environment to verify the proposed method. It is experimentally demonstrated that analog signals retrieved at the receiving end are always of high fidelity using the proposed method, when average path loss (*APL*) is less than 29.0 dB. Only the half number of measurements is used compared to that in conventional methods. The proposed method could open up a novel research perspective for high-fidelity free-space optical analog-signal transmission through dynamic and complex scattering media.

1. Introduction

It is well recognized that information transmission plays an important role in modern society [1,2]. Radio frequency technology has been widely applied in communication systems. However, it has several drawbacks (e.g., small spectral range and license request), and could not fully meet the demands of data communication [2]. Many data transmission approaches have been further developed to address the challenges [3–6]. Among them, free-space optical data transmission has a potential to provide flexible deployments and an extended spectral range, and has attracted much interest [7,8]. However, free-space optical data communication also encounters some significant challenges [9,10]. The atmospheric disturbance, e.g., wind, rain and fog, could severely affect free-space optical data transmission. Optical properties [11–29], e.g., intensity [11–18] and polarization [19–24], could be dynamically changed, when optical transmission is conducted in a turbulent environment. Signal-to-noise ratio of the signals retrieved at the receiving end is severely degraded due to absorption and scattering, and transmission errors are introduced. Some methods [30–34] have been developed to suppress transmission errors induced by atmospheric disturbance. For instance, free-space optical communication could be enhanced using a decision feedback equalizer [32,33] optimized by minimum mean squared error. Until now, few studies have been conducted on optical analog-signal transmission in dynamic and complex scattering environments, and it is desirable to correct the influence induced by

dynamic and complex scattering environments. Non-line-of-sight (NLOS) transmission has also been studied [35–41], and optical wave could be blocked or dramatically attenuated. We have studied to encode a signal into 2D patterns as information carriers [34,42–44] to realize high-fidelity optical transmission, but reference patterns [34] need to be repeatedly used to correct scaling factors in dynamic and complex scattering environments. In addition, four 2D patterns need to be applied to optically transmit each pixel of an analog signal. Therefore, optical analog-signal transmission in dynamic and complex scattering environment is still challenging, and it is desirable to investigate new schemes for high-fidelity free-space optical analog-data transmission through dynamic and complex scattering media.

In this paper, a new scheme is reported to realize high-fidelity free-space optical analog-signal transmission through dynamic and complex scattering media. Each pixel value of original signal is divided into two values. These two values are then encoded into 2D binary arrays using an encoding method and a modified error diffusion algorithm. Each pixel value of original signal is finally transformed into two 2D binary arrays to realize the transmission. Transmission errors and dynamic scaling factors aroused by dynamic and complex scattering media can be temporally corrected. A complex environment composed of dynamic smoke and NLOS is created to verify feasibility of the proposed method. It is experimentally demonstrated that analog signals retrieved at the receiving end are always of high fidelity using the proposed method when average path loss (*APL*) is less than 29.0 dB. The proposed method could offer a research perspective in the realm of free-space optical analog-signal transmission through dynamic and complex scattering media.

2. Principle

2.1. Pixel-to-binary array encoding

In the developed optical analog-signal transmission system, a series of 2D binary arrays are generated to serve as information carriers. A flow chart for the generation of 2D binary arrays is shown in Fig. 1(a). The proposed binary array generation approach is described as follows:

(1) A pixel is enlarged with a given magnification factor M (e.g., 60000) to be a new value b. The integer part of b is denoted as c, and the decimal part of b is denoted as d.

(2) A sequence T with random values is obtained. The length of sequence T is $2 \times c$. The first half of sequence T is generated with random values ranging from 0 to 1, and another half of sequence T is calculated by using the difference between 1 and each corresponding value of the first half part. The sum of T is equal to c.

(3) A 2D array Q of random numbers is generated by arbitrarily placing all the values of sequence T and the decimal value d into a pre-generated all-zero matrix.

(4) A modified error diffusion algorithm is developed to transform the generated 2D array Q obtained in Step (3) into a binary array.

In Step (4), each generated 2D array Q of random numbers is converted into a 2D binary array with a modified error diffusion algorithm, which is described as follows:
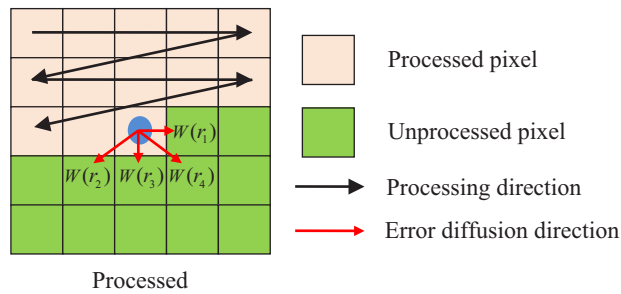
(i) For each pixel in the generated 2D array Q, a threshold of 0.5 is used to transform it into a binary representation (i.e., 0 or 1), which is described by

$$\widehat{q}_i = \begin{cases} 0 & if \ q_i < 0.5 \\ 1 & if \ q_i \geq 0.5 \end{cases}, \tag{1}$$
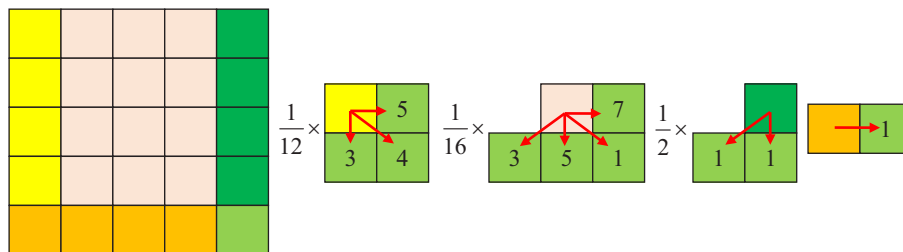
where q_i denotes the ith pixel in the generated 2D array Q and $\widehat{q}_i$ denotes the generated binary value.
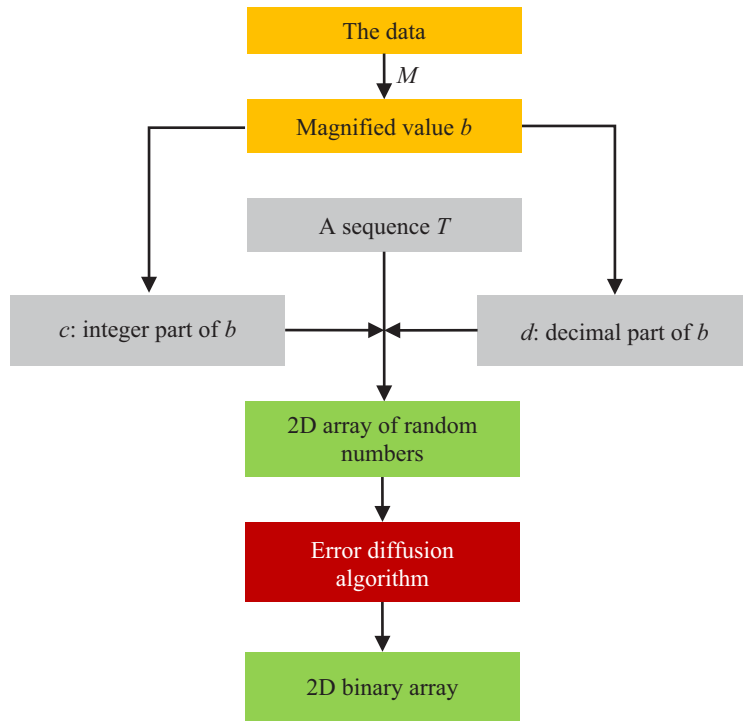
(a)

(b)

(c)

Fig. 1. (a) A flow chart of the proposed binary array generation approach, (b) an error diffusion algorithm, and (c) coefficient distributions in a modified error diffusion algorithm.

(ii) In the error diffusion algorithm [45–47], the difference between the processed pixel value and its binary representation (i.e., 0 or 1) is distributed and added to its neighboring pixels with a certain weighting ratio in each direction, as schematically illustrated in Fig. 1(b). Here, $W(r_1)$, $W(r_2)$, $W(r_3)$ and $W(r_4)$ denote dithering coefficients. The sum of dithering coefficients is equal to 1.

$$W(r_1) + W(r_2) + W(r_3) + W(r_4) = 1. \tag{2}$$

Here, a modified error diffusion algorithm with designed dithering coefficients is used, and four types of dithering coefficients, i.e., (5/12, 3/12, 4/12), (7/16, 3/16, 5/16, 1/16), (1/2, 1/2) and (1) in Fig. 1(c), are correspondingly applied until all pixels in the generated 2D arrays Q are converted into binary. Therefore, the sum of each generated binary pattern can be equal to its corresponding magnified value b in practical applications, e.g., via a flexible adjustment of the magnification factor M with a removal of the decimal part d. According to the proposed pattern generation approach, the generated 2D binary arrays have a proportional relationship with original pixel values, and can be utilized as information carriers to realize optical transmission. Conventional binary matrix (e.g., Walsh-Hadamard matrix and Cake-Cutting Hadamard matrix) is generated by reshaping Hadamard basis into a two-dimensional matrix. Therefore, Hadamard matrices have no direct relationship with original pixel values to be optically transmitted, and may not be suitable.

2.2. Optical data encoding and decoding

In our previous work [34], a reference pattern should be alternately utilized to correct dynamic scaling factors in complex scattering environments, and the transmission of each pixel of an analog signal needs at least four 2D patterns. Here, a new optical encoding scheme with a modified differential method is proposed, and only two 2D binary arrays are required for the transmission of each analog value. A flow chart for the proposed optical data encoding and decoding method is shown in Fig. 2. Assumed that an analog signal to be transmitted contains N pixel values (S_i, $i = 1,2,\ldots,N$), a constant α and a variable β_i ($i = 1,2,\ldots,N$) are used to realize a differential process and a relationship among S_i, α and β_i is given by

$$S_i = \alpha - \beta_i. \tag{3}$$

All values, i.e., α and β_i, are multiplied by the magnification factor M, and then are sequentially encoded into 2D binary arrays (respectively denoted as A and P_i) using the proposed algorithm in Section 2.1. The generated 2D binary arrays are sequentially embedded into a spatial light modulator (SLM) in the developed optical data transmission system. Then, the SLM is illuminated by a collimated light source, and the modulated wave propagates through dynamic and complex scattering media. A series of light intensities corresponding to the 2D binary arrays are recorded by a single-pixel bucket detector [48] at the receiving end. According to wave propagation theory [49,50], the recorded light intensity I_{out} could be described by

$$I_{\text{out}} \approx k|E_{in}|^2, \tag{4}$$

where k denotes a scaling factor and E_{in} denotes the wavefront. The recorded light intensity corresponding to each 2D binary array (i.e., A and P_i) can be respectively described by

$$\begin{aligned} B_{i1} &\approx k(t_i) \iint A(x, y)dxdy \\ &= k(t_i)M\alpha, \end{aligned} \tag{5}$$

$$\begin{aligned} B_{i2} &\approx k(t_{i+1}) \iint P_i(x, y)dxdy \\ &= k(t_{i+1})M\beta_i, \end{aligned} \tag{6}$$
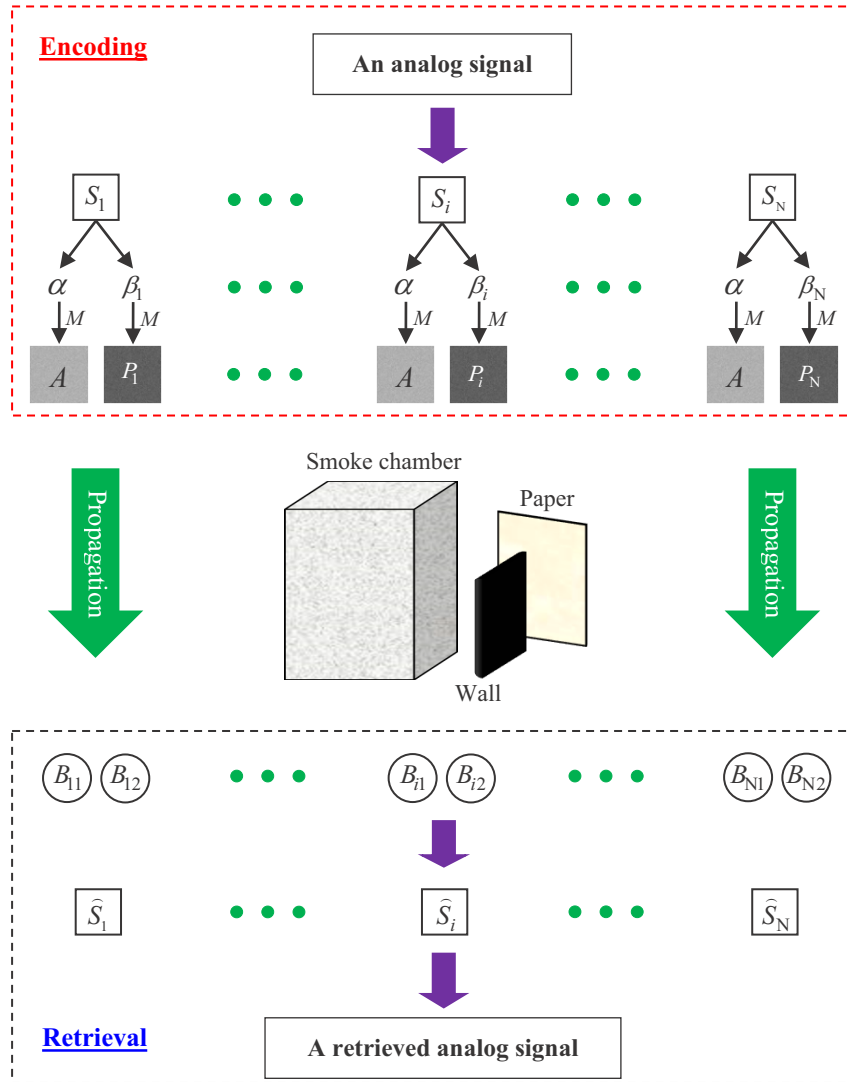
Fig. 2. A flow chart for the proposed method to realize high-fidelity free-space optical analog-signal transmission in dynamic and complex scattering environment. A and P_i ($i = 1,2,...,$N) denote a series of 2D binary arrays obtained by using the proposed algorithm in Section 2.1.

where (x, y) denotes a coordinate, and B denotes light intensity collected by single-pixel detector. At time t_i, the 2D binary array A is embedded into the SLM. At time t_{i+1}, a 2D binary array P_i is embedded into the SLM.

In Eqs. (5) and (6), since t_i is close to t_{i+1}, it can be assumed that two adjacent scaling factors are the same, i.e.,

$$k(t_i) \approx k(t_{i+1}). \tag{7}$$

Therefore, a signal $\widehat{S}_i$ retrieved at the receiving end can be described by

$$\begin{aligned} \widehat{S}_i &= \frac{B_{i1}}{k(t_i)M} - \frac{B_{i2}}{k(t_{i+1})M} \\ &\approx \frac{1}{k(t_i)M}(B_{i1} - B_{i2}) \end{aligned}. \tag{8}$$

Based on Eq. (8), the proposed method can realize high-fidelity free-space optical data transmission in dynamic and complex scattering environments. Each pixel of an analog signal is transformed into two 2D binary arrays for the transmission. After the generated 2D binary pattern is embedded into the SLM, optical field is modulated and its intensity is recorded by using a single-pixel detector at the receiving end. The recorded light intensity has a proportional relationship with the transmitted pixel value.

3. Experimental results and discussion

3.1. Experimental setup

A series of optical experiments are conducted to verify the proposed method. A schematic experimental setup is shown in Fig. 3. A diode-pumped green laser (CrystaLaser, CL532-025-S) is utilized as light source. The laser power is 25.0 mW, and wavelength of the laser is 532.0 nm. The wave is expanded with an objective lens and collimated with a lens. The expanded and collimated wave is reflected by a mirror, and illuminates an amplitude-only spatial light modulator (Holoeye, LC-R720) with pixel size of 20.0 μm. The series of generated 2D binary arrays is sequentially embedded into the SLM to modulate optical wave. The modulated wave propagates through dynamic and complex scattering media. Complex scattering consists of two parts, i.e., dynamic smoke and NLOS. The dynamic smoke is generated in a transparent acrylic chamber. The artificially-generated smoke is produced with a smoke generator (HALFSun, power of 3000 W and pumping rate of 973.0 cm^3/s) and smoke oil. The smoke oil is a mixture of glycerol and water. Around a corner is composed of a wall (i.e., a protective screen) and an A4 paper (a reflective surface). A single-pixel bucket detector (Newport, 918D-UV-OD3R) is used to collect light intensities at the receiving end. No lens is placed before the single-pixel bucket detector. Axial distance d_1 between the SLM and front side of smoke chamber is 30.0 cm, and axial distance d_3 between back side of smoke chamber and A4 paper is 12.0 cm. The distance d_4 between A4 paper and single-pixel bucket detector is 5.0 cm. The dimension of smoke chamber is 30 (L) × 30 (W) × 40 (H) cm^3, and axial distance d_2 is 30.0 cm.

3.2. Attenuations

Dynamic and complex scattering environment in Fig. 3 consists of dynamic smoke and NLOS, and a direct metric to describe the attenuation in free space is optical path loss (*PL*). When each 2D binary array is embedded and displayed, the *PL* can be correspondingly calculated by using incident light intensity and collected light intensity. In optical experiments, the *PL* is calculated to describe dynamic changes in transmission environment, which is described by

$$PL = -10 \times \log_{10} \frac{P_{\mathrm{r}}}{P_{\mathrm{t}}}, \tag{9}$$

where P_t denotes the collected single-pixel light intensity just before smoke chamber and P_r denotes light intensity recorded by single-pixel bucket detector. To eliminate the errors, several
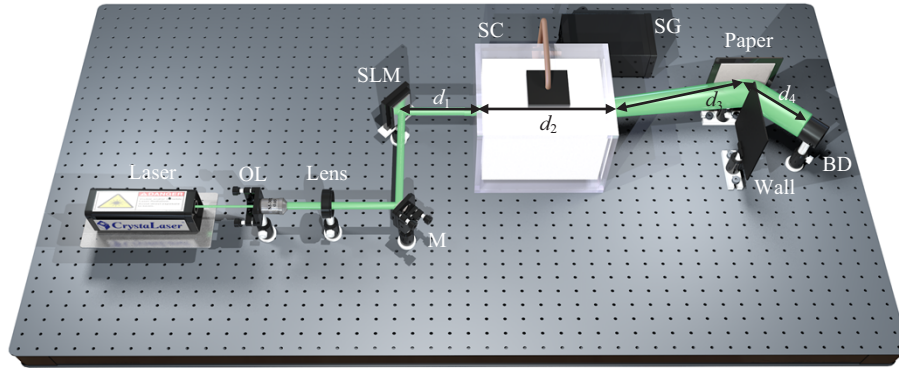
Fig. 3. A schematic experimental setup for the proposed high-fidelity free-space optical data transmission in dynamic and complex scattering environment (i.e., dynamic smoke and NLOS): OL, Objective lens; M, Mirror; SLM, Amplitude-only spatial light modulator; SC, Smoke chamber; SG, Smoke generator; BD, Single-pixel bucket detector.

recordings just before smoke chamber are used to calculate an average incident light intensity described by

$$P_t = \frac{1}{\mathfrak{R}} \sum_{i=1}^{\mathfrak{R}} P_{ti}, \tag{10}$$

where $\mathfrak{R}$ denotes the total number of measurements and P_{ti} denotes collected single-pixel light intensity recorded just before smoke chamber. Here, average incident light intensity P_t is 0.34 mW.

3.3. Experimental results

The pumping rate of smoke generator is 973.0 cm^3/s, and pumping durations can be flexibly adjusted in optical experiments to generate different smoke concentrations in the chamber. Real-time properties in the optical transmission path are shown in Fig. 4(a), when different amount of smoke is respectively pumped into the chamber. The relationships between sampling time and light intensities collected by single-pixel detector are given. The collected light intensities are small at the beginning, and increase with sampling time. Smoke pumped into the chamber has a high concentration at the beginning, and the propagating wave is strongly scattered. When the pumping duration is longer, more smoke is pumped into the chamber. After the liquefaction and sedimentation, the longer pumping duration leads to the larger amount of liquefied smoke adhered to surface of the chamber. The lowest light intensity, i.e., 6.0×10^{-7} W, is obtained at its stable state, when the pumping duration is 50 s. The *PL* changed with sampling time is shown in Fig. 4(b). As sampling time increases, the *PL* decreases due to liquefaction and sedimentation of the smoke in the chamber.

Apart from dynamic smoke, optical data transmission is also affected by the designed NLOS in Fig. 3. Two parameters, i.e., separation distance d and detection angle θ respectively in Figs. 5(a) and 5(b), are analyzed. In optical experiments, default value of the separation distance d is 4.0 cm, and default value of detection angle θ is 45°.

The separation distance d is changed in a range of 0.5 to 6.0 cm, and smoke pumping duration is 30 s. The experimental results are shown in Figs. 6(a) and 6(b). As can be seen in Fig. 6(a), the change trends of recorded light intensities are similar, when different separation distances d are respectively used. As sampling time increases, the recorded light intensities increase due to liquefaction and sedimentation of the smoke in the chamber. When the separation distance
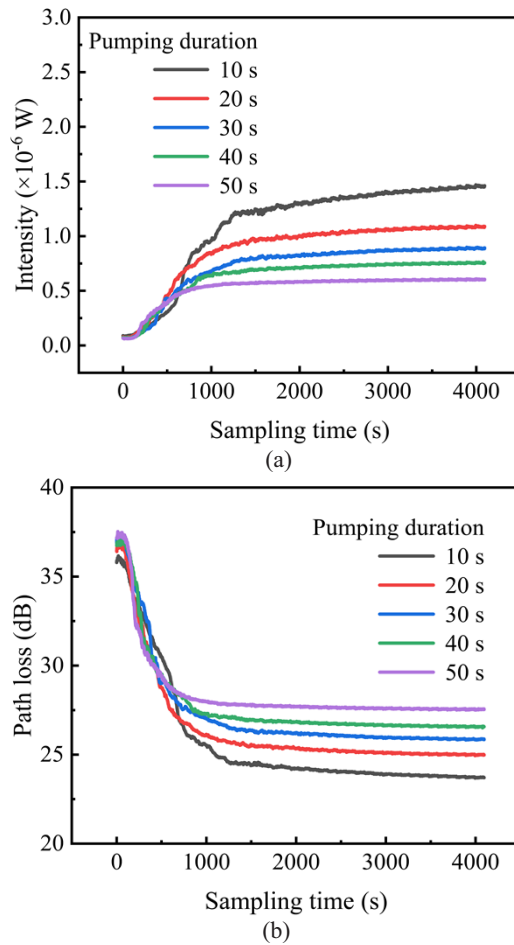
Fig. 4. (a) The relationships between sampling time and optical intensities collected at the receiving end when pumping duration (i.e., 10 s, 20 s, 30 s, 40 s and 50 s) is different, and (b) the relationships between sampling time and the *PL* when pumping duration (i.e., 10 s, 20 s, 30 s, 40 s and 50 s) is different.
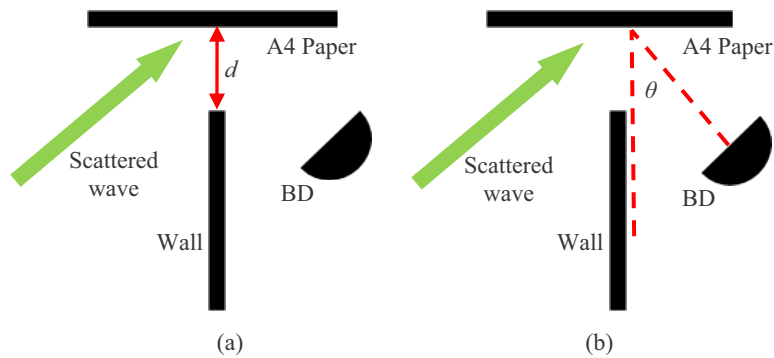

Fig. 5. (a) A schematic of separation distance *d*, ad (b) a schematic of detection angle θ.

around the corner is small (e.g., 0.5 or 0.8 cm), the wall largely blocks the propagating wave, and collected light intensities are significantly reduced. When the separation distance is large (e.g., 4.0 or 6.0 cm), the wall partially blocks the propagating wave. The collected light intensities are close, when the separation distances of 4.0 cm and 6.0 cm are used. The *PL* is also calculated and shown in Fig. 6(b). It is illustrated that the *PLs* are high at the beginning, and decrease with sampling time to remain stable in the end.
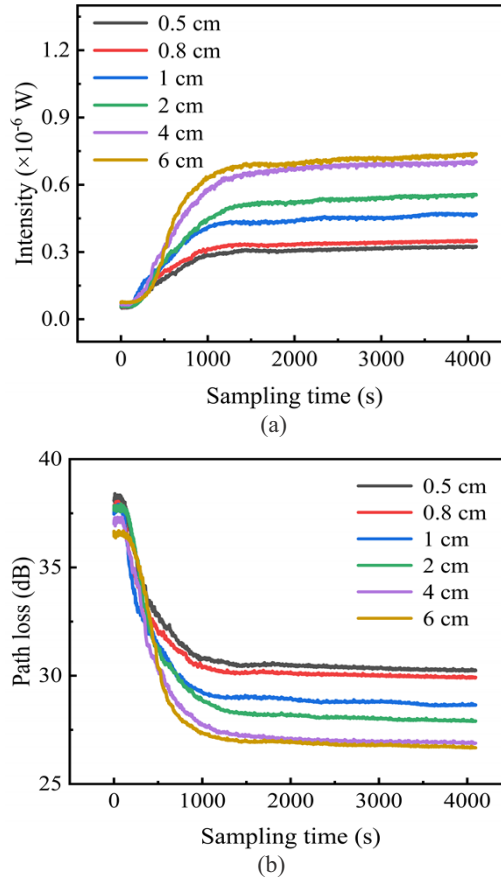

Fig. 6. (a) The relationships between sampling time and light intensities collected at the receiving end when different separation distances (i.e., 0.5 cm, 0.8 cm, 1.0 cm, 2.0 cm, 4.0 cm and 6.0 cm) are respectively used, and (b) the relationships between sampling time and the *PL* when different separation distances (i.e., 0.5 cm, 0.8 cm, 1.0 cm, 2.0 cm, 4.0 cm and 6.0 cm) are respectively used.

The signals retrieved at the receiving end are evaluated by using mean squared error (MSE) and peak signal-to-noise ratio (PSNR), which are respectively calculated by [51]

$$\text{MSE} = \frac{1}{N} \sum_{i=1}^{N} \left(S_i - \widehat{S}_i \right)^2, \tag{11}$$

$$\text{PSNR} = 10\log_{10} \frac{MAX_S^2}{\text{MSE}}, \tag{12}$$

where MAX_S denotes the maximum value of analog signal.

To accurately evaluate dynamic and complex scattering environments, average path loss (*APL*) is further calculated by

$$APL = \frac{1}{2N} \sum_{i=1}^{2N} PL_i, \tag{13}$$

where PL_i denotes the loss obtained when each generated 2D binary array is embedded into the SLM. The typically retrieved analog signals are shown in Figs. 7(a)–7(d), when different separation distances are respectively used. As can be seen in Figs. 7(a)–7(d), high PSNR values and low MSE values can be obtained, which means that the analog signals are retrieved with high fidelity. It is experimentally found that when the separation distance d is larger than 0.5 cm, the proposed method can realize high-fidelity optical analog-signal transmission in dynamic and complex scattering environments.
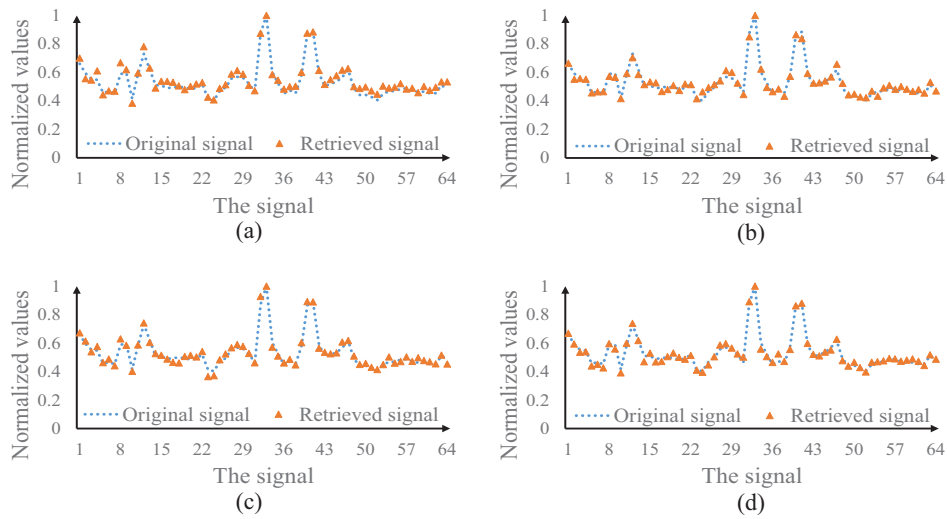

Fig. 7. (a)-(d) The typical signals experimentally retrieved at the receiving end when different separation distances (i.e., 0.5 cm, 0.8 cm, 2.0 cm, and 4.0 cm) are respectively used. The *APL* is 30.76 dB, 30.65 dB, 30.27 dB, and 29.07 dB in (a)-(d), respectively. PSNR values of the retrieved signals in (a)-(d) are 30.14 dB, 32.96 dB, 33.52 dB and 34.68 dB, respectively. MSE values of the retrieved signals in (a)-(d) are 9.68×10^{-4}, 5.06×10^{-4}, 4.44×10^{-4} and 3.40×10^{-4}, respectively.

The detection angle θ around a corner is also studied, and is changed in a range of 0° to 90°. The experimental results are shown in Figs. 8(a) and 8(b), when different detection angles θ, i.e., 0°, 25°, 45°, 65°, and 90°, are respectively used. Here, smoke pumping duration is 30 s. As can be seen in Fig. 8(a), the change trends of recorded light intensities are similar. When the sampling time increases, the recorded light intensities increase due to liquefaction and sedimentation of the smoke in the chamber. When the detection angle θ is 45°, the largest light intensity is collected at the stable state. The *PLs* are also calculated and given in Fig. 8(b). It is illustrated in Fig. 8(b) that the *PL* is high at the beginning, and decreases with sampling time to remain stable in the end.

The typically retrieved signals are shown in Figs. 9(a)–9(d), when detection angle is 0°, 45°, 65° and 90°, respectively. PSNR values of the retrieved signals in Figs. 9(a)–9(d) are 33.95 dB, 37.55 dB, 33.66 dB and 32.42 dB, respectively. MSE values in Figs. 9(a)–9(d) are 4.03×10^{-4}, 1.76×10^{-4}, 4.30×10^{-4} and 5.73×10^{-4}, respectively. It is illustrated in Figs. 9(a)–9(d) that the detection coverage is large at the receiving end, and high mobility and low pointing errors are realized in the developed optical data transmission system.
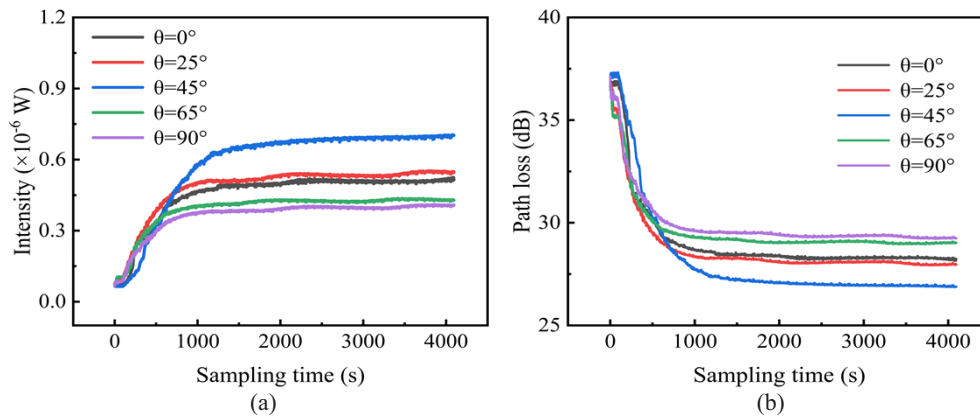
Fig. 8. (a) The relationships between sampling time and light intensities experimentally collected at the receiving end when different detection angles θ (i.e., 0°, 25°, 45°, 65°, and 90°) are respectively used, and (b) the relationships between sampling time and the *PLs* when different detection angles θ (i.e., 0°, 25°, 45°, 65°, and 90°) are respectively used.
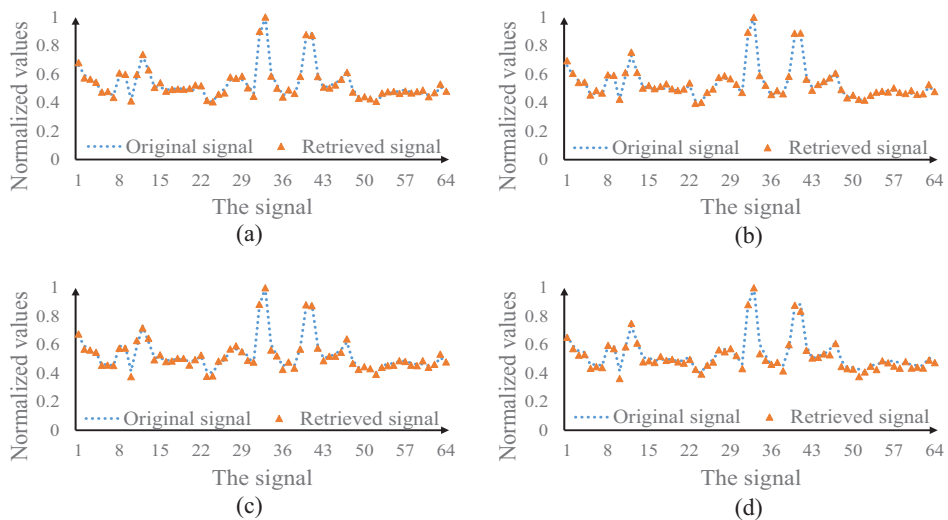

Fig. 9. The typically retrieved analog signals experimentally obtained when the detection angle is (a) 0°, (b) 45°, (c) 65° and (d) 90°. The *APL* is 28.44 dB, 27.19 dB, 29.14 dB, and 29.50 dB in (a)-(d), respectively.

It has been experimentally demonstrated in Figs. 4 and 6–9 that the loss is mainly induced by smoke pumping duration, separation distance and detection angle. A relationship between the *APL* and PSNR values of the retrieved signals is further given in Fig. 10(a). Four irregular analog signals are tested. It is demonstrated in Fig. 10(a) that analog signals retrieved at the receiving end are of high quality, when the *APL* is lower than 29.0 dB. The typical signals retrieved at the receiving end are shown in Figs. 10(b)–10(e). Here, smoke pumping duration is 30 s, and separation distance d is 4.0 cm. The detection angle θ is 45°. PSNR values of the retrieved signals in Figs. 10(b)–10(e) are 35.23 dB, 37.13 dB, 36.01 dB and 35.83 dB, respectively. MSE values of the retrieved signals in Figs. 10(b)–10(e) are 3.00×10^{-4}, 1.94×10^{-4}, 2.51×10^{-4} and 2.61×10^{-4}, respectively. As can be seen in Figs. 10(b)–10(e), the retrieved analog signals are of high fidelity in dynamic and complex scattering environments.
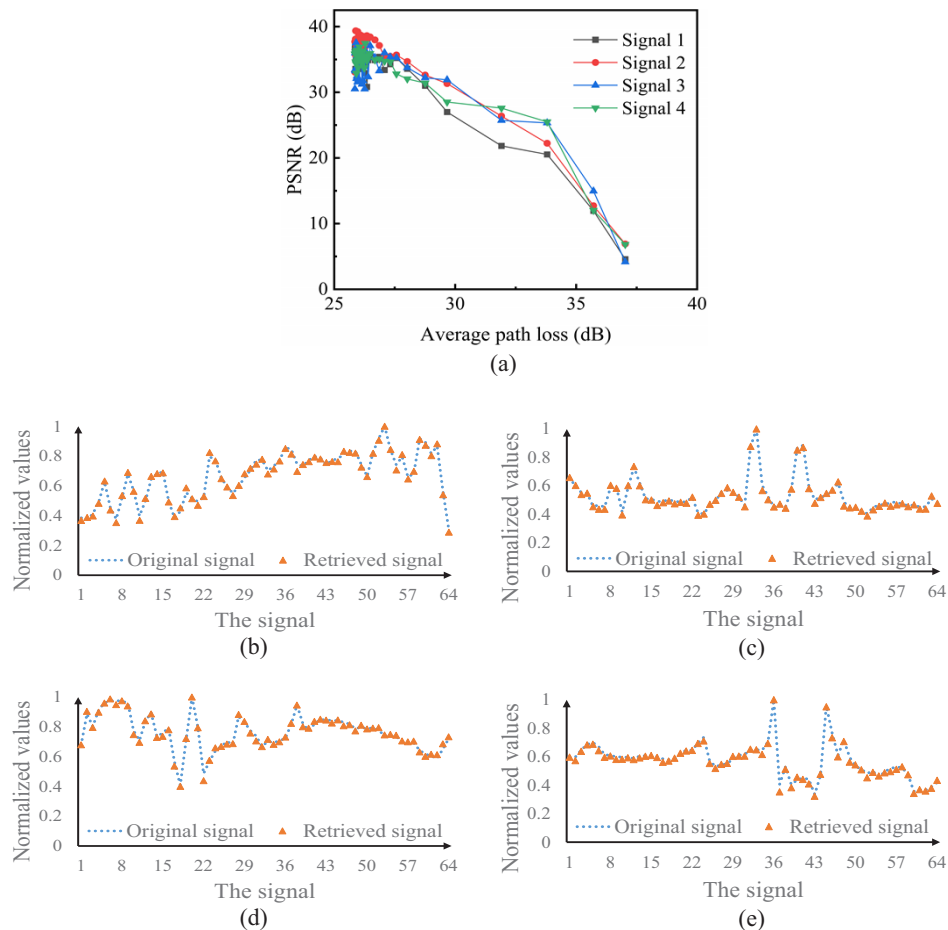

Fig. 10. (a) The relationships between the *APL* and PSNR values of the retrieved signals, and (b)-(e) typical signals retrieved respectively with different *APL*s (i.e., 27.57 dB, 27.61 dB, 27.55 dB, 27.65 dB).

High-fidelity retrieval of the signal can also be realized by applying the generated 2D binary arrays in various scattering environments, e.g., dynamic and turbid water [52]. A SLM is applied in the experiments to modulate optical field. The maximum switching rate of the SLM (e.g., Holoeye, LC-R720) is limited. Digital micro-mirror device (DMD) with a high switching rate

can be used in practice, and the switching rate of a DMD can be up to 22.0 kHz. Therefore, the transmission rate can be enhanced, when the generated 2D binary arrays are used with DMD.

4. Conclusion

A scheme using binary encoding with a modified differential method has been proposed in this paper for realizing high-fidelity analog-signal transmission in dynamic and complex scattering environments. An algorithm is developed to generate a series of 2D binary arrays as information carriers to be used in optical transmission channel. The proposed method employs only two 2D binary patterns for the transmission of each pixel of an analog signal in dynamic and complex scattering environments, and only the half number of measurements is used compared to that in conventional methods. Dynamic scaling factors can be effectively corrected as verified in optical experiments to realize high-fidelity analog-signal retrieval at the receiving end. The proposed method is experimentally demonstrated to provide high-fidelity optical analog-signal transmission, when the *APL* is less than 29.0 dB. The proposed method used in other environments can also be analyzed in our future study. Moreover, the developed temporal correction method could be applied in other areas. The proposed approach could open up a novel research perspective for high-fidelity free-space optical analog-signal transmission through dynamic and complex scattering media.

Disclosures. The authors declare no conflicts of interest.

Data availability. Data underlying the results presented in this paper are not publicly available at this time but may be obtained from the authors upon reasonable request.

References

1. S. Ahmadzadeh, G. Parr, and W. Q. Zhao, "A review on communication aspects of demand response management for future 5 G IoT-based smart grids," IEEE Access **9**, 77555–77571 (2021).
2. S. S. Oyewobi, K. Djouani, and A. M. Kurien, "A review of industrial wireless communications, challenges, and solutions: a cognitive radio approach," Trans. Emerg. Telecommun. Technol. **31**(9), e4055 (2020).
3. J. Wang, J. Y. Yang, I. M. Fazal, N. Ahmed, Y. Yan, H. Huang, Y. Ren, Y. Yue, S. Dolinar, and M. Tur, "Terabit free-space data transmission employing orbital angular momentum multiplexing," Nat. Photonics **6**(7), 488–496 (2012).
4. M. Ijaz, Z. Ghassemlooy, H. Le-minh, S. Zvanovec, J. Perez, J. Pesek, and O. Fiser, "Experimental validation of fog models for FSO under laboratory controlled conditions," in *24th Annual International Symposium on Personal, Indoor, and Mobile Radio Communications* (IEEE, 2013), pp. 19–23.
5. Z. X. He, P. Zhang, D. Wu, X. J. Wu, S. He, J. Wei, X. Y. Gong, T. Wang, D. S. Wang, K. X. Han, S. F. Tong, and H. L. Jiang, "1.7 μm band modulated optical signal transmission through water fog using pump modulated Tm-doped fiber laser," in *Asia Communications and Photonics Conference* (2019), pp. 1–3.
6. S. Q. Hu, H. J. Liu, L. F. Zhao, and X. L. Bian, "The link attenuation model based on Monte Carlo simulation for laser transmission in fog channel," IEEE Photonics J. **12**(4), 1–10 (2020).
7. V. W. Chan, "Free-space optical communications," J. Lightwave Technol. **24**(12), 4750–4762 (2006).
8. M. A. Khalighi and M. Uysal, "Survey on free space optical communication: a communication theory perspective," IEEE Commun. Surveys. Tuts. **16**(4), 2231–2258 (2014).
9. K. Su, L. Moeller, R. B. Barat, and J. F. Federici, "Experimental comparison of performance degradation from terahertz and infrared wireless links in fog," J. Opt. Soc. Am. A **29**(2), 179–184 (2012).
10. W. C. Wang, C. W. Chow, L. Y. Wei, Y. Liu, and C. H. Yeh, "Long distance non-line-of-sight (NLOS) visible light signal detection based on rolling-shutter-patterning of mobile-phone camera," Opt. Express **25**(9), 10103–10108 (2017).
11. Z. Ghassemlooy, H. Le Minh, S. Rajbhandari, J. Perez, and M. Ijaz, "Performance analysis of ethernet/fast-ethernet free space optical communications in a controlled weak turbulence condition," J. Lightwave Technol. **30**(13), 2188–2194 (2012).
12. J. Perez, Z. Ghassemlooy, S. Rajbhandari, M. Ijaz, and H. L. Minh, "Ethernet FSO communications link performance study under a controlled fog environment," IEEE Commun. Lett. **16**(3), 408–410 (2012).
13. M. Ijaz, Z. Ghassemlooy, J. Pesek, O. Fiser, H. L. Minh, and E. Bentley, "Modeling of fog and smoke attenuation in free space optical communications link under controlled laboratory conditions," J. Lightwave Technol. **31**(11), 1720–1726 (2013).

14. B. R. Babaria, T. L. Alvarez, M. T. Bergen, and R. J. Servatius, "Transmission of light in a synthetic fog medium," in *30th Annual Northeast Bioengineering Conference*, (IEEE, 2004), pp. 23–24.

15. P. Lin, T. Wang, W. Ma, Q. Yang, and Z. Liu, "Transmission characteristics of 1.55 and 2.04 μm laser carriers in a simulated smoke channel based on an actively mode-locked fiber laser," Opt. Express **28**(26), 39216–39226 (2020).

16. C. Zhang, J. Zhang, X. Wu, and M. Huang, "Numerical analysis of light reflection and transmission in poly-disperse sea fog," Opt. Express **28**(17), 25410–25430 (2020).

17. M. Ijaz, Z. Ghassemlooy, H. L. Minh, S. Rajbhandari, and J. Perez, "Analysis of fog and smoke attenuation in a free space optical communication link under controlled laboratory conditions," in *International Workshop on Optical Wireless Communications* (IEEE, 2012), pp. 1–3.

18. P. Duthon, M. Colomb, and F. Bernardin, "Light Transmission in Fog: The Influence of Wavelength on the Extinction Coefficient," Appl. Sci. **9**(14), 2843 (2019).

19. X. X. Chen and Z. S. Wu, "Transmission Characteristics of Polarized Light in Low Visibility Fog," in *12th International Symposium on Antennas, Propagation and Electromagnetic Theory* (2018), pp. 1–5.

20. L. Ma, C. Wang, and L. Liu, "Polarized radiative transfer in dense dispersed media containing optically soft sticky particles," Opt. Express **28**(19), 28252–28268 (2020).

21. X. Zeng, X. Chen, Y. Li, and Q. Xiangnan, "Polarization enhancement of linearly polarized light through foggy environments at UV–NIR wavelengths," Appl. Opt. **60**(26), 8103–8108 (2021).

22. S. Zhang, J. T. Zhan, Q. Fu, J. Duan, Y. C. Li, and H. L. Jiang, "Propagation of linear and circular polarization in a settling smoke environment: theory and experiment," Appl. Opt. **58**(17), 4687–4694 (2019).

23. X. W. Zeng, J. K. Chu, W. D. Cao, W. D. Kang, and R. Zhang, "Visible-IR transmission enhancement through fog using circularly polarized light," Appl. Opt. **57**(23), 6817–6822 (2018).

24. S. Zhang, J. Zhan, Q. Fu, J. Duan, Y. Li, and H. Jiang, "Effects of environment variation of glycerol smoke particles on the persistence of linear and circular polarization," Opt. Express **28**(14), 20236–20248 (2020).

25. B. Z. Bentz, B. J. Redman, J. D. van der Laan, K. Westlake, A. Glen, A. L. Sanchez, and J. B. Wright, "Light transport with weak angular dependence in fog," Opt. Express **29**(9), 13231–13245 (2021).

26. B. Wu, B. Marchant, and M. Kavehrad, "Channel modeling of light signals propagating through a battlefield environment: analysis of channel spatial, angular, and temporal dispersion," Appl. Opt. **46**(25), 6442–6448 (2007).

27. P. Qiu, G. Cui, Z. Qian, S. Zhu, X. Shan, Z. Zhao, X. Zhou, X. Cui, and P. Tian, "4.0 Gbps visible light communication in a foggy environment based on a blue laser diode," Opt. Express **29**(9), 14163–14173 (2021).

28. M. S. Awan, P. Brandl, E. Leitgeb, F. Nadeem, L. Csugai-Horvath, and R. Nebuloni, "Transmission of High Data Rate Optical Signals in Fog and Snow Conditions," in *1st International Conference on Wireless Communication, Vehicular Technology, Information Theory and Aerospace and Electronic Systems Technology* (2009), pp. 702–706.

29. J. Perez, S. Zvanovec, Z. Ghassemlooy, and W. O. Popoola, "Experimental characterization and mitigation of turbulence induced signal fades within an ad hoc FSO network," Opt. Express **22**(3), 3208–3218 (2014).

30. J. Libich, J. Perez, S. Zvanovec, Z. Ghassemlooy, R. Nebuloni, and C. Capsoni, "Combined effect of turbulence and aerosol on free-space optical links," Appl. Opt. **56**(2), 336–341 (2017).

31. D. Shah and D. Kothari, "Mitigation of fog and rain effects in free-space optical transmission using combined diversity," in *2nd International Conference on Computer and Communication Technologies* (2015), pp. 725–733.

32. A. Almogahed, A. Amphawan, F. Mohammed, A. Alawadhi, and C. Yuen, "Performance improvement of mode division multiplexing free space optical communication system through various atmospheric conditions with a decision feedback equalizer," Cogent Eng. **9**(1), 2034268 (2022).

33. A. Almogahed, A. Amphawan, and Y. Fazea, "Mitigation of atmospheric turbulences using mode division multiplexing based on decision feedback equalizer for free space optics," J. Opt. Commun. **41**(2), 185–193 (2020).

34. Y. Cao, Y. Xiao, Z. Pan, L. Zhou, and W. Chen, "High-fidelity temporally-corrected transmission through dynamic smoke via pixel-to-plane data encoding," Opt. Express **30**(20), 36464–36477 (2022).

35. Z. Pan, Y. Xiao, L. Zhou, Y. Cao, M. Yang, and W. Chen, "Non-line-of-sight optical information transmission through turbid water," Opt. Express **29**(24), 39498–39510 (2021).

36. A. Assefa, P. J. Chen, X. L. Ho, and J. D. White, "On the potential of solid state LED strips utilizing an organic color converter for non-line of sight visible light communication," Opt. Express **25**(20), 24242–24250 (2017).

37. S. Arnon and D. Kedar, "Non-line-of-sight underwater optical wireless communication network," J. Opt. Soc. Am. A **26**(3), 530–539 (2009).

38. N. B. Hassan, Z. Ghassemlooy, S. Zvanovec, M. Biagi, A. M. Vegni, M. Zhang, and P. Luo, "Non-line-of-sight mimo space-time division multiplexing visible light optical camera communications," J. Lightwave Technol. **37**(10), 2409–2417 (2019).

39. X. Sun, W. Cai, O. Alkhazragi, E. N. Ooi, H. He, A. Chaaban, C. Shen, H. M. Oubei, M. Z. M. Khan, and T. K. Ng, "375-nm ultraviolet-laser based non-line-of-sight underwater optical communication," Opt. Express **26**(10), 12870–12877 (2018).

40. G. Chen, Z. Xu, and B. M. Sadler, "Experimental demonstration of ultraviolet pulse broadening in short-range non-line-of-sight communication channels," Opt. Express **18**(10), 10500–10509 (2010).

41. H. Xiao, Y. Zuo, J. Wu, Y. Li, and J. Lin, "Bit-error-rate performance of non-line-of-sight UV transmission with spatial diversity reception," Opt. Lett. **37**(19), 4143–4145 (2012).

42. Y. Xiao, L. Zhou, and W. Chen, "Wavefront control through multi-layer scattering media using single-pixel detector for high-PSNR optical transmission," Opt. Lasers Eng. **139**, 106453 (2021).

43. Y. Cao, Y. Xiao, Z. Pan, L. Zhou, and W. Chen, "Direct generation of 2D arrays of random numbers for high-fidelity optical ghost diffraction and information transmission through scattering media," Opt. Lasers Eng. **158**, 107141 (2022).

44. Z. Pan, Y. Xiao, Y. Cao, L. Zhou, and W. Chen, "Optical analog-signal transmission and retrieval through turbid water," Appl. Opt. **60**(34), 10704–10713 (2021).

45. V. Ostromoukhov, "A simple and efficient error-diffusion algorithm," In *Proceedings of the 28th Annual Conference on Computer Graphics and Interactive Techniques*, pp. 567–572 (2001).

46. Z. Wang, G. R. Arce, and G. Di Crescenzo, "Halftone visual cryptography via error diffusion," IEEE Trans. Inf. Forensics Secur. **4**(3), 383–396 (2009).

47. R. W. Floyd, "An adaptive algorithm for spatial gray-scale," Proc. Soc. Inf. Disp. **17**, 75–77 (1976).

48. S. Liu, Q. Li, H. Wu, and X. Meng, "Color computational ghost imaging based on a plug-and-play generalized alternating projection," Opt. Express **30**(11), 18364–18373 (2022).

49. B. Judkewitz, R. Horstmeyer, I. M. Vellekoop, I. N. Papadopoulos, and C. Yang, "Translation correlations in anisotropically scattering media," Nat. Phys. **11**(8), 684–689 (2015).

50. E. Tajahuerce, V. Durán, P. Clemente, E. Irles, F. Soldevila, P. Andrés, and J. Lancis, "Image transmission through dynamic scattering media by single-pixel photodetection," Opt. Express **22**(14), 16945–16955 (2014).

51. M. Dehshiri, S. G. Sabouri, and A. Khorsandi, "Structural similarity assessment of an optical coherence tomographic image enhanced using the wavelet transform technique," J. Opt. Soc. Am. A **38**(1), 1–9 (2021).

52. Z. Pan, Y. Xiao, Y. Cao, L. Zhou, and W. Chen, "Optical data transmission through highly dynamic and turbid water using dynamic scaling factors and single-pixel detector," Opt. Express **30**(24), 43480–43490 (2022).